Direct nanoimprinting of moth-eye structures in chalcogenide glass for broadband antireflection in the mid-infrared

Lotz, Mikkel Rønne; Petersen, Christian Rosenberg; Markos, Christos; Bang, Ole; Jakobsen, Mogens Havsteen; Taboryski, Rafael J.

Published in:
Optica

Link to article, DOI:
10.1364/OPTICA.5.000557

Publication date:
2018

Document Version
Publisher's PDF, also known as Version of record

Research Article Vol. 5, No. 5 / May 2018 / Optica 557

Direct nanoimprinting of moth-eye structures in chalcogenide glass for broadband antireflection in the mid-infrared

Mikkel R. Lotz,[1] Christian R. Petersen,[2] Christos Markos,[2] Ole Bang,[2] Mogens H. Jakobsen,[1] and Rafael Taboryski[1,*]

[1]DTU Nanotech, Technical University of Denmark, Kongens Lyngby DK-2800, Denmark
[2]DTU Fotonik, Technical University of Denmark, Kongens Lyngby DK-2800, Denmark
*Corresponding author: rata@nanotech.dtu.dk

Received 7 December 2017; revised 4 April 2018; accepted 10 April 2018 (Doc. ID 314818); published 3 May 2018

Fresnel reflection at the boundary between two media of differing refractive indices is a major contributing factor to the overall loss in mid-infrared optical systems based on high-index materials such as chalcogenide glasses. In this paper, we present a study of broadband antireflective moth-eye structures directly nanoimprinted on the surfaces of arsenic triselenide (As_2Se_3)-based optical windows. Using rigorous coupled-wave analysis, we identify a relief design optimized for high transmittance (<1% reflectance) at 6 μm, which when nanoimprinted features a transmittance improvement ($\Delta T > 12\%$) in the 5.9–7.3 μm spectral range as well as improved omnidirectional properties. Finally, we demonstrate the adaptability of nanoimprinted surface reliefs by tailoring the nanostructure pitch and height, achieving both extremely broadband antireflective and highly efficient antireflective surface reliefs. The results and methods presented herein provide an efficient and scalable solution for improving the transmission of bulk optics, waveguides, and photonic devices in the mid-infrared.

OCIS codes: (120.7000) Transmission; (160.2750) Glass and other amorphous materials; (160.4760) Optical properties; (050.6624) Subwavelength structures; (130.3060) Infrared; (160.4330) Nonlinear optical materials.

https://doi.org/10.1364/OPTICA.5.000557

1. INTRODUCTION

The class of amorphous semiconductors belonging to the chalcogenide glass family exhibits exceptional transparency in the mid-IR region due to its low phonon energy and high optical nonlinearity [1–3]. Moreover, the relatively low glass transition temperature allows for precision glass molding of IR optical elements based on chalcogenide glasses [4–6]. This has enabled numerous chalcogenide glass-based applications, such as chemical sensing [7,8], nonlinear optical devices [9,10], supercontinuum generation [11–15], and thermal imaging [4,6].

Especially the ability to cover both atmospheric transparent windows at 3–5 μm and 7–14 μm as well as the molecular fingerprint region at 6–20 μm has attracted significant attention to these glasses [16]. However, the relatively high refractive index [17] of chalcogenide glasses severely impedes the transmission of light across the air-glass interface due to Fresnel reflection. Attention has therefore been directed towards minimizing Fresnel losses in applications where coupling efficiencies are crucial [18,19]. Unfortunately, in contrast to optical elements in the visible and near-IR range, only a limited number of materials are chemically and thermomechanically compatible with chalcogenide glass, enabling them to be used as effective antireflective (AR) thin-film coatings [20,21]. Furthermore, these materials do not allow the AR properties to be easily and accurately tailored to suit a specific application, such as nonlinear applications, which benefit the most from having the best possible AR efficiency near a specific pump wavelength, or sensing and imaging applications, which benefit from having an ultrabroad bandwidth. A completely new concept introduced by low-cost mid-IR supercontinuum sources using chalcogenide glasses is the requirement to use so-called supercontinuum cascading [22,23], i.e., using one supercontinuum as a pump to generate a new supercontinuum in the chalcogenide fiber. This requires one broadband AR coating on the input facet and another on the output facet of the fiber or waveguide, which is a very tough technological challenge that does not exist in silica fiber-based supercontinuum sources.

To address these shortcomings and technological challenges, different methods of fabricating moth-eye-type surface reliefs have been investigated [24], with ∼99% transmittance between 7 and 12 μm (#R2 in Table 1), being the best reported result for an As_2Se_3 window using the dry-etch fabrication approach [25–27]. However, a major drawback of using the dry-etch fabrication approach is the need for resist lithography to be applied directly onto the glass optics to transfer the AR pattern. A more

Table 1. Measured Peak Transmittance Improvements (ΔT) and Optimum Efficiency Spectra of the Fabricated Surface Reliefs

Sample (#)	P (nm)	H (nm)	Peak ΔT at λ (%)[a]	Optimum Efficiency Spectra (%)
1	900	815 ± 25	12.20 at 3.3 μm	$\Delta T \geq 11$ at 2.8–4.1 μm
2	1000	1075 ± 25	13.28 at 4.6 μm	$\Delta T \geq 12$ at 3.9–5.9 μm
3	1050	1351 ± 10	12.58 at 6.7 μm	$\Delta T \geq 12$ at 5.9–7.3 μm
4	1200	1550 ± 25	12.54 at 7.8 μm	$\Delta T \geq 12$ at 6.8–8.7 μm
R1 [5]	800	N/A	~11[b] at 2.7 μm	$\Delta T \geq 10$ at 2.3–3.5 μm
R2 [26]	2600	4800	~13.22[c] at 7.5 μm	$\Delta T \geq 13$ at 7.0–12 μm

[a]SD ($N = 10$) = ±0.63%.
[b]~61% and ~72% transmission is reported for the blank and imprinted window, respectively.
[c]~99% Single-surface transmission (normalized to the untreated window transmittance assumed to be 78%) is reported for the surface-etched window.

compelling option would be to use direct thermal nanoimprinting to fabricate the AR surfaces. This approach is both cost-effective, as it does not require application of resist with subsequent photolithography, development, and etching to be applied on every workpiece, and is compatible with recently developed molding techniques used for shaping chalcogenide glass lenses [6]. Furthermore, direct nanoimprinting has recently been shown to be a promising method for transfer of AR surface reliefs onto As_2S_3-based optical fiber end facets, significantly reducing coupling losses as well as increasing its laser damage threshold [18,19].

Despite this, only a single preliminary study by MacLeod *et al.* [5] has briefly investigated the transmission properties of direct nanoimprinted bulk As_2Se_3 glass windows, and a thorough inquiry into the relationship between fabrication parameters and transmission is therefore lacking in the literature, a vital topic that we address here, we believe for the first time. In addition, we demonstrate how a truncated ellipsoidal-shaped moth-eye profile imprinted on bulk As_2Se_3, leads to state-of-the-art AR surface reliefs both in terms of bandwidth and AR efficiency.

2. MATERIALS AND METHOD

A. Fabricating the Nickel Shim

The silicon (Si) master and nickel (Ni) shim fabrication process central to this work is outlined in the process flow shown in Fig. 1(a). It begins by spin-coating a 6″ Si wafer with a positive tone deep ultraviolet (DUV)-sensitive photoresist and exposing a master pattern structure comprising a hexagonal array of rounded pillars, as illustrated in Steps 1 and 2 of the process flow. With an inductively coupled plasma reactive ion etching process dominated by physical etching, we subsequently fabricate an array of moth-eye structures in Si (Step 3) and remove any residual photoresist in a subsequent oxygen plasma etch (Step 4). A negative relief Ni mold is then formed by first depositing a nickel-vanadium (NiV) alloy seed layer and subsequently electroforming the Si master structure (Step 5). Separation of the Si master and Ni mold is achieved by submerging it in a potassium hydroxide (KOH) solution, thus etching away the Si and leaving a negative relief mold of Ni (Ni shim) intact (Step 6). Finally, the Ni shim is coated with perfluorodecyltrichlorosilane (FDTS), which acts as an antistiction coating, and is then diced into several smaller and more manageable pieces, like the one shown in Fig. 1(b). In an earlier study, we successfully used a similar shim for the injection molding of almost 1000 polymer chips, a process that is much harsher on the shim than the relative gentle imprinting process applied here [28]. A more detailed account of the parameters used in the shim fabrication process can be found in Supplement 1.

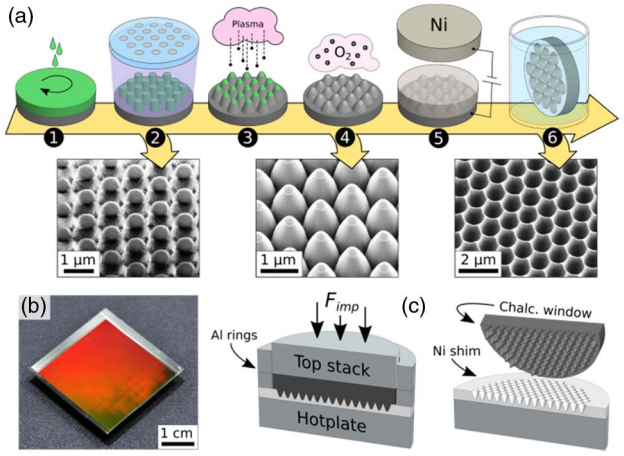

Fig. 1. (a) Ni shim fabrication process flow. 1. Spin-coating resist; 2. DUV lithography; 3. inductively coupled plasma reactive ion etching; 4. oxygen plasma etching; 5. NiV seed layer deposition and Ni electroforming; 6. KOH wet etching and antistiction coating. SEM images at three different stages of fabrication: post-lithography, post-oxygen plasma etching, and post-KOH etching; (b) finished and diced Ni shim; (c) cross-sectional sketch of the custom-made fixture to contain the glass window during nanoimprinting.

B. Nanoimprinting the Chalcogenide Glass Window

In the direct thermal nanoimprinting process, the polished and uncoated stoichiometric As_2Se_3 window (AMTIR-2, Ø 25.4 mm, 2 mm thick) supplied by Amorphous Materials Inc., U.S., is gradually heated up to 210°C over a period of 10 min. As the glass transition temperature of the chalcogenide glass is around 167°C [29], heating it to this temperature significantly lowers the viscosity of the glass to ~10^8 Pa · s [30], making the transfer of a nanoimprint pattern possible. The patterning takes place by incrementally increasing the applied force, F_{imp}, up to around 120 N/cm^2 over a period of 10 min and then subsequently maintaining this force for another 10 min. The window is then cooled down again by heat dissipation in the ambient air, and once the temperature reaches below 150°C, the force is reduced and the moth-eye-patterned window is released, as illustrated in Fig. 1(c). It has recently been reported that a similar nanoimprinting (hot pressing) approach of the same stoichiometric As_2Se_3 at a temperature of 215°C resulted in no observable changes to the composition of the glass [17].

To prevent the chalcogenide glass window from expanding outwards during the imprinting process, the window is placed

in a custom-made fixture comprising a set of aluminum rings and a top stack, as shown in the cross-sectional sketch in Fig. 1(c). The top stack includes a silicone rubber pad, whose role is to ensure a more evenly distributed force, and a sapphire window (WG31050, Thorlabs Inc., U.S.), which ensures a smooth surface against the glass. A more detailed account of the setup and parameters used for the direct thermal nanoimprinting process can be found in Supplement 1.

C. Optical Characterization

The blank and nanoimprinted glass window transmittance is measured and evaluated using a Fourier transform infrared (FTIR) spectrometer (Spectrum 100 FT-IR, PerkinElmer, U.S.). The infrared beam enters the sample compartment through an aperture on the left side and then passes through the sample in the sample holder before exiting through an aperture on the right side of the sample compartment where the detector is located. To measure the sample transmittance at different incident angles, a sample holder with a manually rotating base plate is employed.

A discrepancy between the calculated transmittance (based on the Fresnel equation) and the measured window transmittance was resolved by measuring at a 6° angle of incidence (AOI, θ_i) instead of at normal incidence. This discrepancy is caused by reflected light at the air-glass interface re-entering the spectrometer, thus causing stray light interference. We found the window transmittance measured at 6° AOI to be more consistent and in close agreement with theory. Later in this study, we will show that this systematic error diminishes when calculating the relative transmittance improvement of the nanoimprinted window (see Supplement 1).

3. RESULTS AND DISCUSSION

A. Optimal Surface Relief Dimensions

A simulation modeling approach was adopted to describe the anticipated transmittance of a variety of nanoimprinted air-As_2Se_3 interfaces by utilizing the MATLAB-based modeling software GD-Calc (Grating Diffraction Calculator, KJ Innovation, U.S.). The model computes the diffraction efficiencies of optical grating structures based on the rigorous coupled-wave analysis (RCWA) method [31]. The specific optical grating model employed for this study is shown in Fig. 2(a). The model consists of a single air-glass interface covered with a hexagonal array of rounded moth-eye protrusions. The figure also shows the definition of the pattern pitch and protrusion height, denoted p and h. We chose to model the moth-eye structures with an elliptical profile, as this resembles the types of structures that are typically produced in fabrication. The protruding spheroid is then slightly truncated to resemble the fabricated moth-eye structure shown in the scanning electron microscope (SEM) image in Fig. 1(a). The structure is subsequently stratified, as required by an RCWA-based model, resulting in its sloped sidewalls becoming approximated by a "staircase" design.

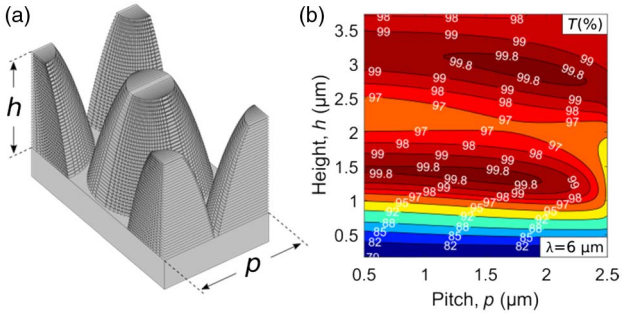

Fig. 2. (a) RCWA model with truncated ellipsoidal-shaped moth-eye structures and whose protrusion height, h, and pattern pitch, p, have also been defined. (b) Simulated 0th order transmittance of a single air-As_2Se_3 interface, at normal incidence and fixed incident wavelength; $\lambda = 6$ μm, using the truncated ellipsoidal protrusion model given in (a).

Figure 2(b) shows a map of the simulated 0th order transmittance at 6 μm and at normal incidence. By mapping the transmittance as a function of p and h, two promising regions in which the modeled surface relief provides a surface reflectance smaller than 1% are revealed: one for a protrusion height of ∼1.4 μm and the other for a protrusion height of ∼3 μm. Since large aspect ratio structures are difficult to transfer successfully with nanoimprinting techniques, the smaller aspect ratio region in the bottom part of the map is preferable. Hence, the range of p and h that best suits our needs for antireflection around 6 μm (in this example case) is found to be at a protrusion height of ∼1.4 μm, with a pitch between 1 and 1.2 μm.

B. Single-Surface Imprint Transmittance

In Fig. 3(a), we show a photograph of the As_2Se_3 windows imprinted with an AR surface relief, and in Fig. 3(b), we show a corresponding SEM image of the moth-eye structure with a pitch size of 1050 nm. The SEM image clearly shows that the moth-eye structures have been successfully transferred onto the glass surface, and only the tips of the protrusions appear to be slightly truncated. To measure the height of the moth-eye structure, we recorded the topographic image shown in Fig. 3(c) using atomic force microscopy (AFM). The red and blue lines in the AFM image indicate the two locations used to extract the height profile line scans given in Fig. 3(d). The reason the two profiles are slightly different is because the base of the structure is not flat, but instead has deeper trenches in the direction of the blue line scan. This feature is difficult to spot in the AFM map shown in Fig. 3(c); however, it is much easier to see in the AFM image of the Ni shim, since this carries the inverted topographic landscape (see Supplement 1). Using the height profiles shown in Fig. 3(d), we extract a protrusion height of 1276 nm from the red profile and 1425 nm from the blue profile, respectively, resulting in a median value of 1350.5 nm. Note that due to tip convolution, the two AFM profiles are expected to be slightly wider than in actuality.

Figure 3(e) shows the measured blank window and imprinted window 0th order transmittance at 6° AOI, together with the analytical blank window 0th order transmittance and the simulated re-creation of the imprinted window 0th order transmittance using RCWA. Since the measured and analytically calculated blank window transmittances are in close agreement, it also allows us to accurately state the theoretical maximum transmittance attainable by a single surface relief (black line), as it is derived from the analytically calculated transmittance (see Supplement 1). Comparing the measured transmittances of the blank and imprinted windows, a clear AR effect is achieved from 2.34 to 14 μm and onwards (see Supplement 1 for the complete spectrum). More importantly, however, the imprinted window exhibits its optimum efficiency from 6.0 to 7.2 μm, where the measured transmittance of the window is greater than 76%

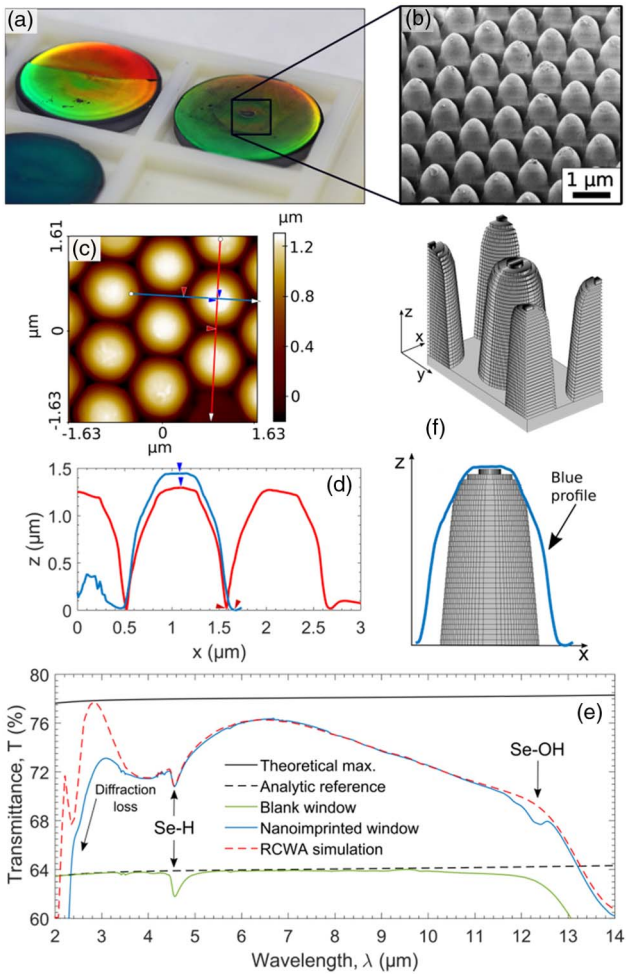

Fig. 3. (a) Photograph of the nanoimprinted As_2Se_3 windows; (b) SEM image of the As_2Se_3 window surface after imprinting a surface relief with a pitch size of 1050 nm, viewed at 30° tilt; (c) AFM image of the surface relief. The red and blue lines indicate the two locations used to extract two height profiles. (d) The two AFM height profiles perpendicular to each other across the same protrusion. The red and blue arrows indicate the points used to extract a protrusion height of 1276 and 1425 nm, respectively. (e) Plot of the measured 0th order transmittance of the nanoimprinted and blank window, together with the simulated window transmittance, the analytically calculated blank window transmittance, and the maximum theoretical window transmittance, all at $\boldsymbol{\theta_i} = 6°$. (f) RCWA model used to produce the simulated transmittance result given in (e).

(up from ~64%). As the calculated theoretical maximum transmittance is ~78%, this roughly corresponds to a reflectance smaller than 2% within this window of optimum efficiency.

A simulation model with a 1050 nm pitch and a protrusion height of 1420 nm, which is very close to the 1425 nm protrusion height measured by AFM, was used to re-create the measured result given in Fig. 3(e). The simulated result fits well with the measured transmittance of the imprinted window, exhibiting a similar and expected drop in the 0th order transmittance at $\lambda \leq 2.92$ μm (based on the 0th order grating condition, $p < \lambda/n$, where n is the refractive index of the substrate [32]), which is where the nanoimprinted relief starts to behave like a diffraction grating at normal incidence, thus explaining the drastic reduction of the 0th order transmittance at wavelengths below ~2.92 μm. The observed drop in the measured transmittance relative to the simulated result near $\lambda \sim 2.92$ μm is likely due to imperfections in the relief, such as defects that cause scattering and that become nonnegligible when λ and p are comparable in size. We captured a minor example of a relief defect in the AFM image, which had a pattern vacancy due to a missing protrusion (not shown).

The simulation model and the moth-eye profile captured in the blue line scan match up well, as shown in Fig. 3(f), with the exception of the width, which is slightly larger in the AFM profile, which we believe can be explained by tip convolution, and, to some extent, defects in the sample, which render the effective fill fraction smaller. However, keep in mind that in order to obtain a precise correlation between the model and observed moth-eye structures, the imprint would have to be completely homogeneous.

1. Surface Oxidation

Aside from a few minor water absorption bands at 2.9 μm and at 5.5–7.5 μm as well as absorption peaks at 4.3 μm and 15 μm attributed to atmospheric CO_2, we observe two distinct absorption peaks at 4.55 and 12.3 μm, as indicated in Fig. 3(e), which correspond to Se-H and Se-OH absorption bands, respectively. The Se-H band appears in both the nanoimprinted and blank window transmittance spectra, and it is therefore inferred that this impurity is introduced during glass synthesis and not during the nanoimprint process heat treatment. For the Se-OH impurities, we see that while they do not appear in the blank window transmittance spectra shown in Fig. 3(e), we have since also observed similar oxidation of the untreated chalcogenide glass windows after longer storage under ambient conditions. However, no Se-OH absorption was observed in the measurements performed immediately after nanoimprinting the windows, suggesting that the heat treatment merely triggers an accelerated oxidation growth, which subsequently takes place as the chalcogenide glass windows are stored in ambient air. Similar observations of sample deterioration due to oxidation have also been reported in studies regarding other chalcogenide compounds [33–35]. This hypothesis is also consistent with preliminary tests to nanoimprint in an inert atmosphere (N_2), in which no change to the accelerated oxidation growth has been observed.

C. Transmittance Improvement as Function of AOI

One of the most important features of AR surface reliefs is the ability to maintain their effectiveness across a wide range of incident angles, which is useful for many practical applications. By calculating the improvement to the window transmittance after receiving a nanoimprinted surface relief, denoted ΔT, we also get a very insightful figure of merit to evaluate its AR efficiency relative to its initial conditions. Calculating this figure of merit for the measured transmittance of the nanoimprinted window given in Fig. 3(e) as AOI is increased, we obtain the plots shown in Fig. 4(a). This shows us that the previously described window has a transmittance improvement of $\Delta T > 12\%$ in the 5.9–7.3 μm spectral range at both 0° and 6° AOI. A more modest improvement of $\Delta T > 7.7\%$ is accomplished in the 2.8–10.7 μm spectral range. Since the calculated improvements at normal and at 6° AOI are almost identical, the previously documented discrepancy at normal incidence is minimized when considering the relative improvement of the transmittance.

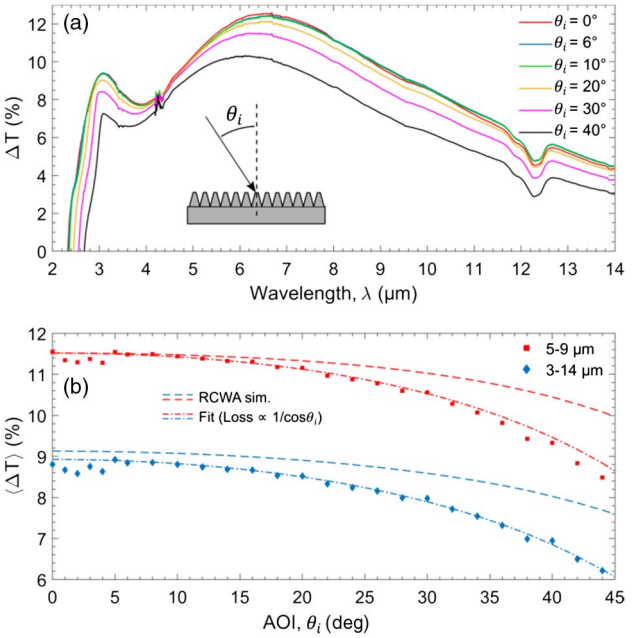

Fig. 4. (a) Plot of the transmittance improvement, ΔT, as function of AOI (θ_i), based on the measured transmittance of the nanoimprinted window shown in Fig. 3. (b) The average transmittance improvement, $\langle \Delta T \rangle$, as a function of AOI, averaged across the 3–14 μm and 5–9 μm spectral ranges, plotted together with the RCWA simulation and a curved fit. The inset sketch illustrates how AOI is defined.

We therefore assume that for measurements done at $\theta_i < 6°$, we can still calculate the corresponding transmittance improvement and obtain a reasonably accurate metric.

The average transmittance improvement, denoted $\langle \Delta T \rangle$ for the same surface relief, is plotted in Fig. 4(b) as a function of AOI. The figure presents two sets of data; in the first data set, we average the improvement from 5 to 9 μm, thus mainly covering the optimum transmission spectrum; meanwhile, in the second data set, the averaging range is broadened to include 3–14 μm. In the 5–9 μm spectrum, the average improvement is about 11.5% at normal and close to normal incidence, while in the broader 3–14 μm spectrum, this is about 9%. As the AOI increases, the surface relief maintains an average improvement >10% for $\theta_i < 35°$ in the 5–9 μm spectral range, whereas in the 3–14 μm spectral range an average improvement >8% for $\theta_i \leq 30°$ is maintained. The deviation in the data points at AOI < 6° is caused by the systematic discrepancy addressed earlier.

Simulating the transmittance as a function of AOI using the RCWA model given in Fig. 3(f) and comparing it to the two measured data sets, we see a rather large deviation between the two as the AOI increases. Assuming that the simulation model is an accurate model description of the fabricated surface relief, then the deviation suggests a transmission loss in the measurement. While the observed offset between the average improvement in the 3–14 μm spectral range and the simulated result can be explained by the previously noted drop in measured transmittance near the boundary where the grating changes behavior to a diffraction grating, the measured data points generally appear to have a stronger dependency on the AOI, exhibiting an angle dependent loss not included in the simulation model. The root cause for the transmission loss remains unresolved; however, we found a decent fit to the two data sets by adding identical loss terms proportional to $1/\cos(\theta_i)$ to the two simulation results. This suggests that the transmission loss is related to absorption by a surface oxide layer, as the optical thickness of such a layer follows the same dependency to AOI. This fits well with our previous observations, which suggest the presence of surface oxidation on the surface. However, other loss mechanisms, such as scattering or the area probed changing size with AOI (from a circle to an ellipse, thus possibly probing a less optimal surface relief) cannot strictly be excluded from impacting the measurement either.

D. Tailoring the Surface Relief

Besides the surface relief studied in the previous sections, an assortment of other reliefs, which had a variety of different pitch sizes and corresponding protrusion heights, were also tested. The SEM images of the tested surface reliefs are presented in Figs. 5(a)–5(d), including the relief previously studied and discussed (surface relief #3). The height disparity between the different surface reliefs is given in Table 1 and is primarily a result of a difference in etch rate caused by aspect ratio-dependent etching (ARDE [36]), introduced during the Si master fabrication step.

Measuring the transmittance and subsequently calculating the corresponding transmittance improvement of the nanoimprinted surface reliefs, we obtain the plots shown in Fig. 5(e), the results of which are summarized in terms of individual peak efficiency and optimum spectrum in Table 1. The figure demonstrates the sensitivity to pitch size and protrusion height that surface reliefs have, and how changing them translates to vastly different AR characteristics, which is a trait that can be utilized to tailor the surface relief to suit a specific application.

With the smallest height of just 815 ± 25 nm, surface relief #1 is tailored to generate a considerable peak transmittance improvement of $\Delta T = 12.2\%$ at 3.3 μm; however, it is too small to support substantial broadband antireflection. With an optimum efficiency spectrum spanning 2.8 to 4.1 μm, this surface relief is ideal for handling the emission from a high-power mid-IR

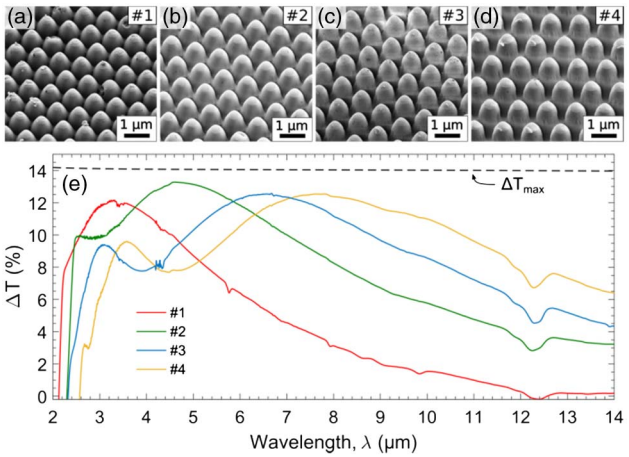

Fig. 5. (a)–(d) SEM images of As_2Se_3 windows after receiving a surface relief with a different pitch and protrusion heights, viewed at the same magnification and 30° tilt; (e) calculated transmittance improvement of the nanoimprinted windows, corresponding to a transmittance measured at normal incidence. ΔT_{max} indicates the boundary for the theoretical maximum transmittance improvement attainable by a single-surface relief in As_2Se_3.

holmium- or erbium-doped ZBLAN (ZrF_4-20BaF_2-4LaF_3-3AlF_3-20NaF)-based fiber laser system, which operates in the 2.7–2.9 μm spectral range [37,38]. Surface relief #4 has the tallest fabricated moth-eye protrusions, which measure 1550 ± 25 nm in height, and as a consequence, the relief features extremely broadband antireflection and achieves $\Delta T > 7.7\%$ between 3.2 and 12 μm. Surface relief #2 exhibits the highest recorded peak transmittance improvements of $\Delta T = 13.28\%$ at 4.6 μm, corresponding to ∼0.8% reflectance at the surface. This is anticipated, as its surface relief dimensions (p and h) can be traced back to a similar highly efficient region on a simulated transmittance map using a 4.5 μm incident wavelength (see Supplement 1). With optimum efficiency spectra located at 3.9–5.9 μm and 5.9–7.3 μm, respectively, surface reliefs #2 and #3 provide AR properties that are extremely useful at the input facet of chalcogenide fiber-based mid-IR supercontinuum light sources, such as the two demonstrations presented by Petersen *et al.* [12], which utilize pumping with intense ultrashort pulses at a central wavelength of 4.5 and 6.3 μm. Likewise, surface relief #4, with its extremely broad AR bandwidth, could potentially be useful on the output facet of this optical system, as it could facilitate a higher output intensity of the generated supercontinuum light exiting the fiber.

Surface relief #4 could potentially also be used in thermal imaging applications, as its transmittance improvement extends out to 14 μm, thus covering the thermal imaging window (9–14 μm). However, for such imaging applications, the fabrication process must be optimized to reduce the number of pattern defects leading to scattering, which affects the image quality [24]. Since the diffraction and scattering losses in surface relief #4 primarily manifest at the shorter wavelengths between 3 and 4 μm in the transmittance spectrum, the level of scattering in the thermal imaging window should be negligible, assuming the number of defects is kept low.

Comparing the summary of our results shown in Table 1 with the state-of-the-art nanoimprinted AR surface relief (#R1 in Table 1), it is evident that the surface reliefs fabricated in this work deliver a level of performance that exceeds that of the previous generation, both in terms of their applicable range and in terms of their baseline efficiency (ΔT), which is more than 1%–2% higher than the previous. Compared to the state-of-the-art dry-etched AR surface relief (#R2 in Table 1), we achieve about the same peak transmittance improvement, but with a considerably smaller optimum spectrum, likely because of the much smaller moth-eye structures. The reproducibility of the technique was checked by imprinting on two batches of chalcogenide glasses using the same shims after four months and achieving very similar results. Nevertheless, the current results constitute a substantial improvement to nanoimprinted reliefs in chalcogenide glass that rival the AR performance of dry-etched surface reliefs.

4. CONCLUSIONS

We have demonstrated a direct thermal nanoimprinting method capable of rapidly patterning the surfaces of bulk chalcogenide glass materials with highly efficient broadband AR surface reliefs. Utilizing a modeling approach, we were able to design a surface relief layout and subsequently pattern it, providing nanoimprinted surface replicas with excellent optical characteristics. With peak improvements to the window transmittance between 12.2% and 13.28%, corresponding to a 0.7%–1.8% reflectance on the imprinted surface, the presented peak efficiency of the nanoimprinted reliefs is substantial and on par with what has been achieved with dry-etched surface reliefs. We believe that the method demonstrated here paves the way for faster and more cost-effective ways of fabricating tailor-made AR surfaces directly onto chalcogenide-based optical passive components such as lenses, windows, and optical fibers.

Funding. Det Frie Forskningsråd (DFF) (4184-00359B); Innovation Fund Denmark (4107-00011A).

Acknowledgment. We thank Nikolaj Kofoed Mandsberg for his input on the theory as well as many fruitful discussions.

See Supplement 1 for supporting content.

REFERENCES

1. R. Frerichs, "New optical glasses with good transparency in the infrared," J. Opt. Soc. Am. **43**, 1153–1157 (1953).
2. B. J. Eggleton, B. Luther-Davies, and K. Richardson, "Chalcogenide photonics," Nat. Photonics **5**, 141–148 (2011).
3. T. Wang, X. Gai, W. H. Wei, R. P. Wang, Z. Y. Yang, X. Shen, S. Madden, and B. Luther-Davies, "Systematic z-scan measurements of the third order nonlinearity of chalcogenide glasses," Opt. Mater. Express **4**, 1011–1022 (2014).
4. X. H. Zhang, Y. Guimond, and Y. Bellec, "Production of complex chalcogenide glass optics by molding for thermal imaging," J. Non-Cryst. Solids **326**, 519–523 (2003).
5. B. D. MacLeod, D. S. Hobbs, and E. Sabatino, "Moldable AR microstructures for improved laser transmission and damage resistance in CIRCM fiber optic beam delivery systems," in *Conference on Window and Dome Technologies and Materials XII*, Orlando, Florida (2011).
6. D. H. Cha, H. J. Kim, Y. Hwang, J. C. Jeong, and J. H. Kim, "Fabrication of molded chalcogenide-glass lens for thermal imaging applications," Appl. Opt. **51**, 5649–5656 (2012).
7. B. Bureau, C. Boussard, S. Cui, R. Chahal, M. L. Anne, V. Nazabal, O. Sire, O. Loreal, P. Lucas, V. Monbet, J. L. Doualan, P. Camy, H. Tariel, F. Charpentier, L. Quetel, J. L. Adam, and J. Lucas, "Chalcogenide optical fibers for mid-infrared sensing," Opt. Eng. **53**, 027101 (2014).
8. A. B. Seddon, N. S. Abdel-Moneim, L. Zhang, W. J. Pan, D. Furniss, C. J. Mellor, T. Kohoutek, J. Orava, T. Wagner, and T. M. Benson, "Mid-infrared integrated optics: versatile hot embossing of mid-infrared glasses for on-chip planar waveguides for molecular sensing," Opt. Eng. **53**, 071824 (2014).
9. M. D. Pelusi, V. G. Ta'eed, L. B. Fu, E. Magi, M. R. E. Lamont, S. Madden, D. Y. Choi, D. A. P. Bulla, B. Luther-Davies, and B. J. Eggleton, "Applications of highly-nonlinear chalcogenide glass devices tailored for high-speed all-optical signal processing," IEEE J. Sel. Top. Quantum Electron. **14**, 529–539 (2008).
10. V. G. Ta'eed, N. J. Baker, L. B. Fu, K. Finsterbusch, M. R. E. Lamont, D. J. Moss, H. C. Nguyen, B. J. Eggleton, D. Y. Choi, S. Madden, and B. Luther-Davies, "Ultrafast all-optical chalcogenide glass photonic circuits," Opt. Express **15**, 9205–9221 (2007).
11. B. Zhang, Y. Yu, C. C. Zhai, S. S. Qi, Y. W. Wang, A. P. Yang, X. Gai, R. P. Wang, Z. Y. Yang, and B. Luther-Davies, "High brightness 2.2–12 μm mid-infrared supercontinuum generation in a nontoxic chalcogenide step-index fiber," J. Am. Ceram. Soc. **99**, 2565–2568 (2016).
12. C. R. Petersen, U. Moller, I. Kubat, B. B. Zhou, S. Dupont, J. Ramsay, T. Benson, S. Sujecki, N. Abdel-Moneim, Z. Q. Tang, D. Furniss, A. Seddon, and O. Bang, "Mid-infrared supercontinuum covering the 1.4–13.3 μm molecular fingerprint region using ultra-high NA chalcogenide step-index fibre," Nat. Photonics **8**, 830–834 (2014).
13. Z. M. Zhao, B. Wu, X. S. Wang, Z. H. Pan, Z. J. Liu, P. Q. Zhang, X. Shen, Q. H. Nie, S. X. Dai, and R. P. Wang, "Mid-infrared supercontinuum covering 2.0–16 μm in a low-loss telluride single-mode fiber," Laser Photon. Rev. **11**, 1700005 (2017).
14. C. R. Petersen, R. D. Engelsholm, C. Markos, L. Brilland, C. Caillaud, J. Troles, and O. Bang, "Increased mid-infrared supercontinuum bandwidth

and average power by tapering large-mode-area chalcogenide photonic crystal fibers," Opt. Express **25**, 15336–15347 (2017).
15. T. L. Cheng, K. Nagasaka, T. H. Tuan, X. J. Xue, M. Matsumoto, H. Tezuka, T. Suzuki, and Y. Ohishi, "Mid-infrared supercontinuum generation spanning 2.0 to 15.1 μm in a chalcogenide step-index fiber," Opt. Lett. **41**, 2117–2120 (2016).
16. G. Steinmeyer and J. S. Skibina, "Supercontinua entering the mid-infrared," Nat. Photonics **8**, 814–815 (2014).
17. Y. Fang, D. Jayasuriya, D. Furniss, Z. Q. Tang, L. Sojka, C. Markos, S. Sujecki, A. B. Seddon, and T. M. Benson, "Determining the refractive index dispersion and thickness of hot-pressed chalcogenide thin films from an improved Swanepoel method," Opt. Quantum Electron. **49**, 237 (2017).
18. R. J. Weiblen, C. R. Menyuk, L. E. Busse, L. B. Shaw, J. S. Sanghera, and I. D. Aggarwal, "Optimized moth-eye anti-reflective structures for As_2S_3 chalcogenide optical fibers," Opt. Express **24**, 10172–10187 (2016).
19. J. Sanghera, C. Florea, L. Busse, B. Shaw, F. Miklos, and I. Aggarwal, "Reduced Fresnel losses in chalcogenide fibers by using anti-reflective surface structures on fiber end faces," Opt. Express **18**, 26760–26768 (2010).
20. E. Brinley, S. Seal, R. Folks, E. Braunstein, and L. Kramer, "High efficiency SiO_2-TiO_2 hybrid sol-gel antireflective coating for infrared applications," J. Vac. Sci. Technol. A **24**, 1141–1146 (2006).
21. S. Shabahang, F. A. Tan, J. D. Perlstein, G. Tao, O. Alvarez, F. Chenard, A. Sincore, L. Shah, M. C. Richardson, K. L. Schepler, and A. F. Abouraddy, "Robust multimaterial chalcogenide fibers produced by a hybrid fiber-fabrication process," Opt. Mater. Express **7**, 2336–2345 (2017).
22. I. Kubat, C. R. Petersen, U. V. Moller, A. Seddon, T. Benson, L. Brilland, D. Mechin, P. M. Moselund, and O. Bang, "Thulium pumped mid-infrared 0.9–9μm supercontinuum generation in concatenated fluoride and chalcogenide glass fibers," Opt. Express **22**, 3959–3967 (2014).
23. C. R. Petersen, P. M. Moselund, C. Petersen, U. Moller, and O. Bang, "Spectral-temporal composition matters when cascading supercontinua into the mid-infrared," Opt. Express **24**, 749–758 (2016).
24. G. J. Tan, J. H. Lee, Y. H. Lan, M. K. Wei, L. H. Peng, I. C. Cheng, and S. T. Wu, "Broadband antireflection film with moth-eye-like structure for flexible display applications," Optica **4**, 678–683 (2017).
25. D. S. Hobbs, B. D. MacLeod, and J. R. Riccobono, "Update on the development of high performance anti-reflecting surface relief microstructures," in *Conference on Window and Dome Technologies and Materials X*, Orlando, Florida (2007).
26. D. S. Hobbs, "Laser damage threshold measurements of anti-reflection microstructures operating in the near UV and mid-infrared," in *42nd Annual Laser Damage Symposium*, Boulder, Colorado (2010).
27. M. Silvennoinen, K. Paivasaari, J. J. J. Kaakkunen, V. K. Tikhomirov, A. Lehmuskero, P. Vahimaa, and V. V. Moshchalkov, "Imprinting the nanostructures on the high refractive index semiconductor glass," Appl. Surf. Sci. **257**, 6829–6832 (2011).
28. P. F. Ostergaard, J. Lopacinska-Jorgensen, J. N. Pedersen, N. Tommerup, A. Kristensen, H. Flyvbjerg, A. Silahtaroglu, R. Marie, and R. Taboryski, "Optical mapping of single-molecule human DNA in disposable, mass-produced all-polymer devices," J. Micromech. Microeng. **25**, 105002 (2015).
29. Amorphous Materials Inc., "AMTIR-2 data sheet," http://www.amorphousmaterials.com (accessed April 20, 2018).
30. Y. Zou, D. N. Zhang, H. T. Lin, L. Li, L. Moreel, J. Zhou, Q. Y. Du, O. Ogbuu, S. Danto, J. D. Musgraves, K. Richardson, K. D. Dobson, R. Birkmire, and J. J. Hu, "High-performance, high-index-contrast chalcogenide glass photonics on silicon and unconventional non-planar substrates," Adv. Opt. Mater. **2**, 478–486 (2014).
31. K. Han and C. H. Chang, "Numerical modeling of sub-wavelength anti-reflective structures for solar module applications," Nanomaterials **4**, 87–128 (2014).
32. W. H. Southwell, "Pyramid-array surface-relief structures producing antireflection index matching on optical surfaces," J. Opt. Soc. Am. A **8**, 549–553 (1991).
33. T. Kohoutek, J. Orava, A. L. Greer, and H. Fudouzi, "Sub-micrometer soft lithography of a bulk chalcogenide glass," Opt. Express **21**, 9584–9591 (2013).
34. J. J. Hu, N. Carlie, N. N. Feng, L. Petit, A. Agarwal, K. Richardson, and L. Kimerling, "Planar waveguide-coupled, high-index-contrast, high-*Q* resonators in chalcogenide glass for sensing," Opt. Lett. **33**, 2500–2502 (2008).
35. J. J. Hu, N. N. Feng, N. Carlie, L. Petit, A. Agarwal, K. Richardson, and L. Kimerling, "Optical loss reduction in high-index-contrast chalcogenide glass waveguides via thermal reflow," Opt. Express **18**, 1469–1478 (2010).
36. J. Yeom, Y. Wu, J. C. Selby, and M. A. Shannon, "Maximum achievable aspect ratio in deep reactive ion etching of silicon due to aspect ratio dependent transport and the microloading effect," J. Vac. Sci. Technol. B **23**, 2319–2329 (2005).
37. S. Antipov, D. D. Hudson, A. Fuerbach, and S. D. Jackson, "High-power mid-infrared femtosecond fiber laser in the water vapor transmission window," Optica **3**, 1373–1376 (2016).
38. R. I. Woodward, D. D. Hudson, A. Fuerbach, and S. D. Jackson, "Generation of 70-fs pulses at 2.86 μm from a mid-infrared fiber laser," Opt. Lett. **42**, 4893–4896 (2017).